R. Yan, N. Masood (Corresponding Author), T. K. Saha, F. Bai and Huajie Gu, "The Anatomy of the 2016 South Australia Blackout: A Catastrophic Event in a High Renewable Network", IEEE Transactions on Power Systems, Vol. 33, No. 5, pp. 5374-5388, September, 2018. DOI: 10.1109/TPWRS.2018.2820150

The Anatomy of the 2016 South Australia Blackout: A Catastrophic Event in a High Renewable Network

Ruifeng Yan, *Member, IEEE*, Nahid-Al-Masood, *Member, IEEE*, Tapan Kumar Saha, *Senior Member, IEEE*, Feifei Bai, *Member, IEEE* and Huajie Gu, *Student Member, IEEE*

***Abstract*— Over the last decade, many power systems have significantly changed with the proliferation of renewable generation sources such as wind and solar photovoltaic (PV). Due to their variability and non-synchronous nature, new challenges and complexities have emerged regarding operational security of modern power systems. The 2016 South Australia (SA) blackout was the first known blackout due to such a high renewable situation. An official report has recently been published to review the causes and provide the corresponding recommendations for improvement of network operation, control and security. However, there are still a number of critical issues and debates which remain unsolved, such as network bottleneck identification, over-voltage explanation, pole slip concern, frequency dip mystery, and frequency/voltage instability debate. In this paper, based on the reconstruction of the event, these unsettled issues are prudently analyzed to unveil their root causes. In addition, an innovative scheme is proposed to prevent the blackout by identifying the network separation at an early stage. This research will not only further advance the understanding of the 2016 SA blackout but also will provide valuable guidelines for the management of future renewable-rich networks.**

***Index Terms*-- blackout, high renewable penetration, wind and PV, frequency response.**

I. Introduction

ALMOST every large power system around the world has experienced major blackouts at some point in history [1, 2]. For example, from the year 2000 to date, major blackouts occurred in North America, Scandinavia and Italy in 2003 [3], Brazil in 2009 and 2011 [4], India in 2012 [5], and Turkey in 2015 [6]. Whenever there is a blackout, business, industry, transportation and communication are adversely affected, and eventually the blackout causes significant social, economic and even political consequences. Therefore, a thorough examination after each blackout is always required for further improvement on power system security, planning, operation and control. As a major blackout event, the 2016 South Australia (SA) blackout should be comprehensively investigated as well. However, unlike previous incidents, the SA blackout happened under the conditions of high renewable penetration with very low system inertia, which has posed new challenges for modern network management. It is worth mentioning that the SA 2016 event is the first known blackout incident in a renewable prolific network.

A. Background

On 28th September 2016, a severe storm smashed SA and damaged several remote transmission towers late in the afternoon, and subsequently the SA grid lost around 52% of wind generation within a few minutes. This deficit had to be fulfilled by the power import from the neighbouring state – Victoria (VIC) through the Heywood AC interconnection. However, such an increased power flow was beyond the capability of the interconnection. Ultimately, the SA network was separated from the rest of the Southeast Australian network and collapsed soon afterwards. This state-wide major blackout sent around 1.7 million people [7] into darkness and resulted in a financial loss of approximately 367 million Australian Dollars [8].

With around 2,900 MW peak load [9], SA has developed approximately 1,600 MW wind [10] and 730 MW photovoltaic (PV) generation [11]. Right before the blackout event, wind and PV power provided almost 50% of the total demand in SA, while conventional synchronous generation only accounted for 17.6%, and the rest came from the interconnection [12]. Therefore, the proliferation of renewable energy in SA was accused by some sectors for this catastrophic blackout. Such criticism will hinder further development of renewable resources, which will result in moving away from meeting the national renewable energy target in Australia

B. Sequence of Events and Investigation Progress of the SA Blackout

In order to explicitly describe the sequence of events during the blackout, a network closely resembling the high voltage network of SA is used as a reference, which is illustrated in Fig. 1 [13].

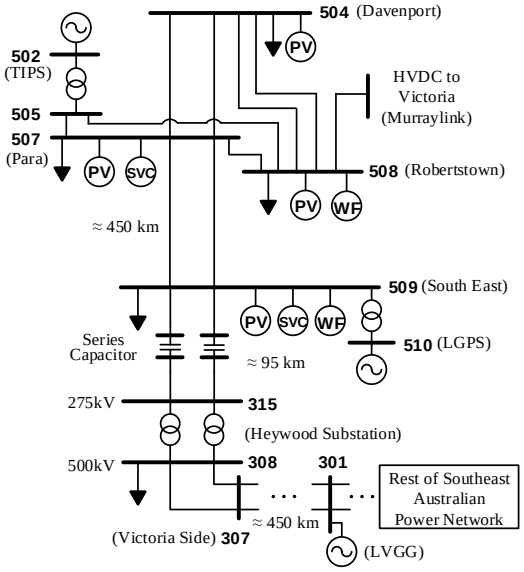

Fig. 1 Network closely resembles the South Australia power grid [13]

The Australian Energy Market Operator (AEMO)

Corresponding author Nahid-Al-Masood is with the Department of EEE, Bangladesh University of Engineering and Technology, Dhaka 1205, Bangladesh, and also with the School of IT & Electrical Engineering, The University of Queensland, Brisbane, QLD 4072, Australia (e-mail: nahidal.masood@uqconnect.edu.au).

Ruifeng Yan, Tapan Kumar Saha, Feifei Bai and Huajie Gu are with the School of IT & Electrical Engineering, The University of Queensland, Brisbane, QLD 4072, Australia (e-mail: ruifeng@itee.uq.edu.au, saha@itee.uq.edu.au, f.bai@uq.edu.au, h.gu@uq.edu.au).

published an official report [12] for the 2016 SA blackout. First, a number of network faults were caused by a thunderstorm. Among them, most of the uncleared faults were located far from load centers, generators and interconnection, so the integrity of the network was not significantly affected. However, this triggered disconnection of a number of wind farms (located at Bus 508), because these wind plants had set a limit of two-to-six faults per minute in their control systems. As a result, there was a sustained wind power reduction of 456 MW.

Meanwhile, the SA synchronous reserve was very low, so the resultant power deficit had to be provided through the interconnection. Consequently, this caused an excessive power flow between VIC and SA (from Bus 315 to Bus 507), which exceeded the angular stability limit. Therefore, loss of synchronism relays located at Bus 509 towards Bus 315 operated that led to a network separation. Nevertheless, even under this situation, the SA network was expected to survive by itself via appropriate load shedding mechanism [14]. However, in reality it did not withstand such a separation, because the rate of change of frequency (ROCOF) was too high for activating under frequency load shedding (UFLS) to reestablish a power balance. Rapidly, the grid frequency dropped below the synchronous machine tripping threshold (47 Hz) causing cascading generator tripping and eventually a state-wide blackout. The recorded frequency and voltage profiles at various locations (such as Para – Bus 507, South East – Bus 509, Heywood – Bus 315, Davenport – Bus 504 and Robertstwon – Bus 508) are shown in Fig. 2. These frequency and voltage traces depict the progression of the blackout from the power system point of view.

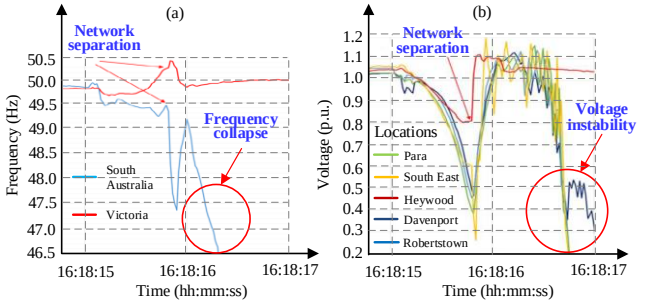

Fig. 2 2016 South Australian blackout (a) Frequency collapse (b) Voltage instability [12]

C. Research Gaps and Foci

A significant amount of effort has been placed on the analysis of the blackout event since it happened. However, there are still some major questions left to be answered, which are summarized as follows.

(1) *Identification of network bottleneck:* Due to the recent development of wind farms at Bus 509, the new operating scenarios may emerge. Consequently, the location of the network bottleneck may vary from time to time. Eventually, it introduces following research questions- i) how may the network bottleneck change during various operating conditions? and ii) how can the actual network bottleneck that eventually restricted the interconnection flow and caused subsequent network separation during the SA blackout be identified? In addition, the voltage traces from different locations were in a downward trend and separated at different time during network separation [Fig. 2(b)]. For example, at first the Bus 315 (Heywood) voltage trace was separated from the others, which was then followed by the voltage trace of Bus 509 (South East). Furthermore, voltage at different buses reduced to different levels. For instance, voltage at Bus 315 reduced to 0.8 pu, whereas the voltages at Bus 509 and Bus 507 (Para) decreased to around 0.6 pu and 0.4 pu respectively before the separation. Especially, the voltage at Para (within the capital city Adelaide – the load center) was significantly lower than the South East region. It instigates one critical question- how can such voltage profiles be analyzed? Analysis of the voltage behavior will not only help to determine the network bottleneck but also provide valuable information regarding the SA grid strength.

(2) *Over-voltage issue after network separation*: After the network separation, two synchronous generators in Ladbroke Grove Power Station (LGPS) were disconnected due to over-voltage, which left only three synchronous machines in Torrens Island Power Station (TIPS) to battle the critical separation event. The AEMO report states such over-voltage is consistent with the historical observation of similar events. However, the reasons for over-voltage are not yet explained.

(3) *High ROCOF induced pole slip concern*: According to the AEMO report for the period after network separation, the average ROCOF was as high as 6 Hz/s, and two out of three TIPS units were disconnected due to unknown lock-out protection. Some have expressed the concern of generator pole slip under high ROCOF, because 2 Hz/s can be the limit for pole slip as indicated in the KEMA report [15]. Nevertheless, there is no firm conclusion so far for this speculation.

(4) *UFLS malfunction due to frequency dip*: After the network separation [Fig. 2(a)], there was a mysterious frequency dip (around 47.5 Hz), and soon afterwards a frequency surge followed. Such a frequency trace can potentially trigger UFLS timer and then quickly reset the timer as the measured frequency recovered. Once the frequency drop re-triggered the UFLS timer again, there was not enough time any more for the operation of UFLS to save the SA network. The AEMO report mentioned the sudden voltage angle changes and rapid load variations may be the reasons for such a frequency shape, however, the true causes are still not clear.

(5) *Frequency/Voltage instability debate*: After the network separation, what is the root cause for the blackout – frequency or voltage instability or a combination of them? This subject has been continuously debated within local power industries, because the root cause needs to be understood first to provide further directions for potential solutions. Yet, there is no answer to this issue.

This paper intends to bridge these gaps by reconstructing the blackout event based on the available data, and subsequently examining the root causes of the above identified major issues through network dynamic simulation and analysis. This research clarifies the critical and yet unexplained concerns on the 2016 SA blackout, which can provide invaluable experience and insight for system operators in managing high renewable networks (but not necessarily only limited to SA). Moreover, the proposed solutions can also serve as a guideline and pave the way to develop necessary prevention techniques to avoid similar blackouts in future.

II. Pre-event South Australia Power Network and Modeling Implication

A. Pre-Event Operating Condition

In this sub-section, the conditions before the 2016 SA blackout (referred to as pre-event) are introduced to set a background for further presentation. As shown in Fig. 1, South Australia is connected to Victoria through two interconnections. One of them is the 275 kV high voltage AC (HVAC) Heywood interconnection (between Bus 315 and Bus 509 in Fig. 1) and the other is the 165 kV high voltage DC (HVDC) Murraylink interconnection. Murraylink is a Voltage Source Converter (VSC) link, which operates in a constant power mode. Therefore, it does not provide any frequency response during disturbances.

It can be seen from Fig. 1 that Heywood (Bus 315) is connected to Para (Bus 507) through a double-circuit transmission line through South East (Bus 509), with approximately 95 km from Heywood to South East and 450 km from South East to Para. In order to maintain voltages to a satisfactory level, two Static VAR Compensators (SVCs) were installed in Para and South East substations. Further, to increase the transfer capability of the Heywood interconnection, the transmission line was reconfigured with 50% series compensation.

In the pre-event operation (Table I), 3 synchronous generators in TIPS (Bus 502) and 2 in LGPS (Bus 510) were committed. The rated capacities of each TIPS and LGPS unit are 200 MW and 40 MW respectively. The total synchronous generation at Bus 502 and 510 was 250 MW and 80 MW respectively in the pre-blackout condition. Therefore, the corresponding capacity factor (the ratio between total generation and total installed capacity) of TIPS and LGPS was approximately 41.67% and 100%.

The total wind generation was around 883 MW distributed in Roberstown and South East (Bus 507 and Bus 509), and the behind-meter PV generation was approximately 50 MW. In addition, power imports via Heywood and Murraylink interconnections were 500 MW and 113 MW respectively. The total load including loss was recorded as 1,826 MW, where Para substation (Bus 507) contains a major portion as it is close to the capital city Adelaide. It is evident from this profile that the pre-event SA system operated with a high penetration of wind and PV, and only 5 synchronous machines. This increased the difficulty for the SA grid to control its network stability (both frequency and voltage) following the loss of Heywood interconnection.

TABLE I
PRE-EVENT POWER GENERATION PROFILE IN SA [12]

Source	Generation (MW)
Synchronous generators	330
Wind	883
PV (behind-meter)	50
Import from Victoria via Heywood	500
Import from Victoria via Murraylink	113
Total load (including losses)	1826

B. Frequency Calculation

During large disturbances and fast transients, the rotors of different generators may have very different speeds. Under such conditions, the system frequency temporarily becomes a local parameter despite its global nature in steady state. Therefore, measuring the frequency at a specific single node in the grid following a disturbance can be ambiguous. In order to address this issue, an expression of equivalent system frequency, f (also known as center of frequency) shown in (1) is introduced in the literature [16]. This expression is adopted to remove the small variations in the measured frequencies.

$$f = \frac{\sum_{i=1}^{i=n}(S_i \times H_i \times \omega_i)}{\sum_{i=1}^{i=n}(S_i \times H_i)} \quad (1)$$

where S_i is the rating of i-th synchronous generator (in MVA), H_i denotes the inertia constant of i-th synchronous generator (in s), ω_i is the speed of i-th synchronous generator (in pu) and n is the total number of committed synchronous generators.

In a real system, for synchronous machines, frequency is measured from their rotor speeds. For any other components (e.g. relays, meters etc.), frequency is mostly measured via Phase Locked Loop (PLL), which is based on voltage wave shapes. However, PLL may result in inaccuracy during fast transient events.

In this paper, PSCAD/EMTDC (Power System Computer Aided Design/Electromagnetic Transients including DC) is deployed as a simulation tool [17]. In this tool, frequency is estimated using the same approaches as of a real system (i.e. measured rotor frequency for synchronous machines and calculated frequency from PLL for other components).

C. Model Validation

The actual measurement data during the SA blackout are available in the report [12] published by AEMO. These data were recorded using high-speed monitoring devices, and are regarded as the most accurate evidence of the state of the system during the blackout [12]. The relevant data from [12] are utilized to replicate the blackout event in the PSCAD/EMTDC simulation platform. Since PSCAD/EMTDC uses EMT-type models, it is most appropriate for simulating the time domain electromagnetic responses of power systems. Therefore, this software serves as a suitable platform for investigating the SA blackout.

After reconstruction of the SA blackout in the simulation environment, different parameters such as voltage, frequency, interconnection flow, synchronous generation, wind generation etc. are compared with the actual records. To demonstrate the validity of the simulation models, two important indicators namely voltage and frequency are taken into account.

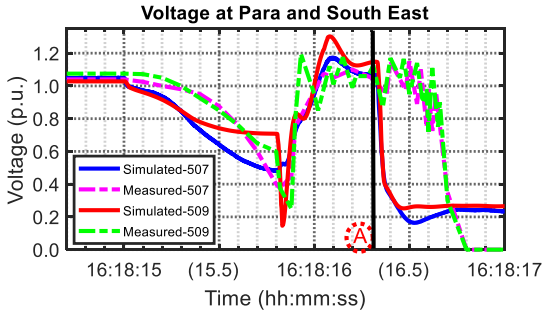

Fig. 3 Comparison between simulated and measured voltages

Voltages at two key locations in SA – Para (Bus 507) and South East (Bus 509) are illustrated in Fig. 3 as examples. It can be seen that until point A, the simulated voltages closely match the actual measured data. However, after point A, there are reasonable mismatches between simulated and measured voltages. This is because after point A, the SA frequency dropped below 47 Hz. As a result, cascading tripping of all the synchronous generators occurred, and

eventually the system encountered a blackout. Thereby, after point A, SA was no more a valid power system. Consequently, any data beyond point A are incomprehensible numerical values from recording devices and the simulation tool. Therefore, these data do not have any implication and can be disregarded.

Furthermore, simulated frequencies of SA and VIC are compared with the corresponding measured values. As shown in Fig. 4(a), the simulated frequencies approximately conform to the actual records for both systems. In addition, LGPS experienced momentary over frequency after the network separation. Comparing the simulated and measured frequency traces depicted in Fig. 4(b), it can be said that the over frequency phenomenon at LGPS is also replicated.

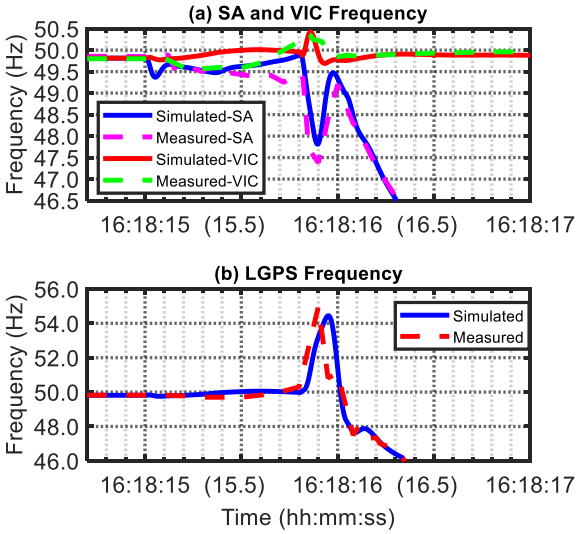

Fig. 4 Comparison between simulated and measured frequencies

From the above discussions, it can be revealed that the simulated voltage and frequency curves closely match the actual records. Therefore, the simulation models can be trusted for further analyses. In addition, it is to be clarified that real recorded data are presented in Table I and Fig. 2. On the other hand, Figs. 3 and 4 contain data from both simulations and actual records. Furthermore, the analysis results presented in the subsequent sections are obtained from simulations.

D. Impact of Inertia on Network Frequency Response

Owing to the substantial penetration of wind power, the total inertia in SA has considerably decreased. Such a reduction of system inertia has a noticeable impact on the network frequency response, which needs to be thoroughly analyzed for a better and clear understanding. To this end, a simulation case is considered as an example where 500 MW Heywood interconnection tripping contingency is applied in the SA grid. Furthermore, different inertia levels are taken into account for a comparison study.

Frequency response is assessed via two indicators – frequency nadir and ROCOF. Frequency nadir is the lowest point in the frequency excursion curve that can be determined from (1). On the other hand, ROCOF (in Hz/s) specifies the initial rate of frequency decline, which is given by (2).

$$ROCOF = \frac{1}{2} \times \frac{\Delta P \times f_0}{IR} \quad (2)$$

where ΔP is the contingency size (in MW), IR denotes the total inertia (in MWs) and f_0 refers to the nominal frequency (in Hz).

Fig. 5 represents the frequency nadir and ROCOF for different inertia values. It can be observed that as inertia decreases, frequency nadir deteriorates. In addition, ROCOF increases due to a decrease of system inertia. Following this trend, ROCOF after the network separation may become very high in a renewable-prolific network. Consequently, the frequency would rapidly drop below the synchronous machine tripping threshold (47 Hz). Therefore, UFLS scheme may not get sufficient time to be activated to stop the frequency excursion. Eventually, it would cause cascading tripping of all the generators. As a result, the whole network would encounter a blackout. Therefore, compared to a traditional power system, the risk of blackout in a renewable-rich network considerably increases due to the reduction of system inertia.

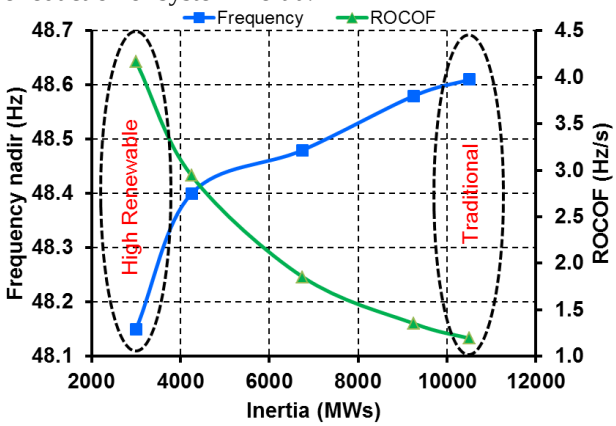

Fig. 5 Frequency response performance for various inertia levels

E. Role of Governors in Primary Frequency Regulation

Prior to the blackout, three synchronous generator units in TIPS were online. As shown in Fig. 6, each TIPS unit offered less than 10 MW governor response until the network separation at 16:18:15.8 (point A). Afterwards, following the network separation, the rapid drop in system frequency did not allow sufficient time to noticeably increase the active power outputs from these units. Therefore, the role of TIPS generators in primary frequency regulation was negligible during the SA blackout event.

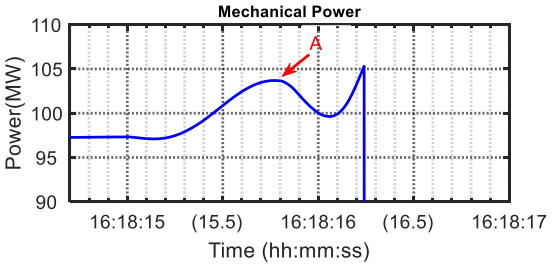

Fig. 6 Governor response of a TIPS unit

In addition, two units in LGPS did not provide any governor response before the network separation as they were running at their rated capacities. Furthermore, both units tripped due to over-voltage after the network separation. Therefore, the LGPS units did not participate in primary frequency regulation at all.

F. Response of Murraylink during the SA Blackout

The Murraylink HVDC shown in Fig. 1 is based on VSC technology. According to the technology provider – ABB [18, 19], the Murraylink converter has a reactive power range of [-160MVAR ~ 140MVAR], but this range in the inverter mode will be reduced to [-100MVAR ~ 100MVAR]

at its rated active power of 220 MW. Because the Murraylink HVDC is located in a remote and weak grid, the AC voltage control (achieved through converter reactive power regulation) will be continuously active in order to maintain an adequate voltage level for real power transmission.

The response speed of the Murraylink HVDC to voltage disturbances is designed to be very fast – generally less than 20 ms [12], which means the Murraylink HVDC will start to inject reactive power for voltage regulation as soon as disturbance occurs. During the network separation of the 2016 SA blackout, the terminal AC voltage of the Murraylink was very low (less than 0.5 pu). Consequently, the HVDC converter quickly reached its reactive power limit, but still it was not able to have much impact on the voltage magnitude. As a result, real power transfer across the Murraylink decreased by more than 50% [12].

G. Impact of Load Models

In this paper, for dynamic simulations, active power is modeled as constant current load. In contrast, reactive power is modeled as constant impedance load. However, essentially both real and reactive power can be represented through a number of alternative approaches as well. Typical approaches include constant impedance (Const. *Z*), constant current (Const. *I*) and constant power (Const. *P*) models. In order to investigate the implication of different load models, nine probable combinations as shown in Table II are sequentially taken into account.

From dynamic simulations, it is found that for all nine cases, the network separation occurs and ultimately the SA network encounters a blackout. Therefore, it can be concluded that different load models do not have a noticeable impact on the fate of the SA network on 28th September 2016.

TABLE II
IMPLICATION OF VARIOUS LOAD MODELS

Real power	Reactive power	SA network situation
Const. *Z*	Const. *Z*	Blackout
	Const. *I*	
	Const. *P*	
Const. *I*	Const. *Z*	Blackout
	Const. *I*	
	Const. *P*	
Const. *P*	Const. *Z*	Blackout
	Const. *I*	
	Const. *P*	

III. ANALYSIS OF RESEARCH GAPS

Virtually, the network separation and blackout may again happen due to several unpredictable events, such as trip of a large generator, a transmission line and a transformer, and intermittency of wind and PV generation. Therefore, it is necessary to investigate the research gaps identified in Section I Part C for a better and complete understanding of the current issues, and providing the direction for further correction regarding operation and control of the SA network.

A. Identification of Network Bottleneck

In the past, the generation and load at Bus 509 were insignificant. Thus, the transmission line from Bus 315 to Bus 507 was virtually treated as a direct connection. In addition, major generators in Victoria side (Latrobe Valley Generator Group – LVGG at Bus 301) were located at around 450 km away from Bus 315. Therefore, the distance from the generation (Bus 301) to main load center (Bus 507 – Para) was approximately around 995 km. To mitigate the bottleneck of such a long line (i.e. 301– 315 – 509 – 507), series compensation was implemented in the middle of the double circuit line between Bus 315 and Bus 509 (Fig. 1) [20].

Due to the recent installation of wind power plants at Bus 509, the network may operate under various conditions from time to time. For example, if the wind generation at Bus 509 is higher than its local load, the net power is fed into the network. As a result, the power flow in 509 – 507 is more than that of 315 – 509 (during power import from Victoria to South Australia). Under such a scenario, 301– 315 – 509 – 507 line cannot be regarded as a simple series connection any more. Consequently, the location of the network bottleneck may change.

During the 2016 SA blackout, due to the wind farm trip in the Robertstown (Bus 508) area, the real power transfer from VIC to SA as formulated in (3) drastically increased. When the required power exceeded the angular stability limit (when the voltage angle difference $\delta_{V_{509-507}} = 90°$), the system integrity can no longer be sustained. Therefore, the loss of synchronism relays located in South East towards the Bus 315 side were triggered to isolate the SA region.

$$P_{509-507} \cong \frac{|\overrightarrow{V_{509}}|\cdot|\overrightarrow{V_{507}}|}{X_{509-507}} \cdot \sin(\delta_{V_{509-507}}) \qquad (3)$$

During this separation process as shown in Fig. 7 (a), the voltage magnitude of Bus 507 dropped much more significantly than that of Bus 509. In addition, the voltage angles swung in the opposite directions, and a more substantial decrease of the voltage angle of Bus 507 was observed. In order to analyze the voltage profiles during the network separation, a voltage vector trajectory method is developed to more intuitively determine the electrical center. This method is based on the traditional R-X impedance trajectory method for system protection design [21, 22].

Fig. 7(b) illustrates the voltage-vector diagram of Bus 507 (Para) and Bus 509 (South East). The blue vector triangle with a superscript of t_0 represents the pre-event condition. The vector from $\vec{V}_{507}^{t_0}$ to $\vec{V}_{509}^{t_0}$ describes the voltage differences along the transmission line from Bus 509 to Bus 507, which is shown by (4).

$$\vec{V}_{509}^{t_0} - \vec{V}_{507}^{t_0} = \vec{I}^{t_0} \cdot Z \cdot D \qquad (4)$$

where Z is the line impedance per km (pu/km) and D is the line distance in km. From the origin E, a random vector can be drawn to any point on vector $\vec{V}_{507}^{t_0}\vec{V}_{509}^{t_0}$, e.g. $\overrightarrow{EA}$. Then, $\overrightarrow{EA}$ denotes the point A voltage on the line with a certain distance away from Bus 509, where the distance is proportional to the magnitude of $\vec{A}\,\vec{V}_{509}^{t_0}$ with respect to $\vec{V}_{507}^{t_0}\vec{V}_{509}^{t_0}$ regarding the total line distance D. For instance, if the point A is located in the middle of the vector $\vec{V}_{507}^{t_0}\vec{V}_{509}^{t_0}$, then $\overrightarrow{EA}$ is the voltage vector of the middle point of the line. In addition, if the vector $\overrightarrow{EA}$ is perpendicular to the vector $\vec{V}_{507}^{t_0}\vec{V}_{509}^{t_0}$, then $\overrightarrow{EA}$ is the shortest vector, denoting the lowest voltage point ($V_{L_{min}}^{t_0}$) along the line. These interpretations are based on a reasonable assumption that the impedance is equally distributed along the whole transmission line.

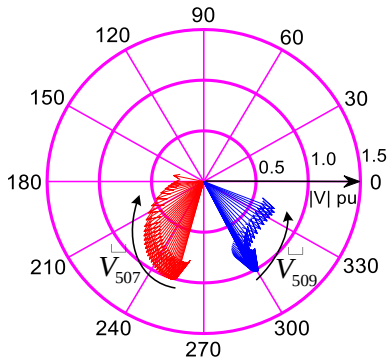

(a) Voltage-vector traces of Buses 507 and 509

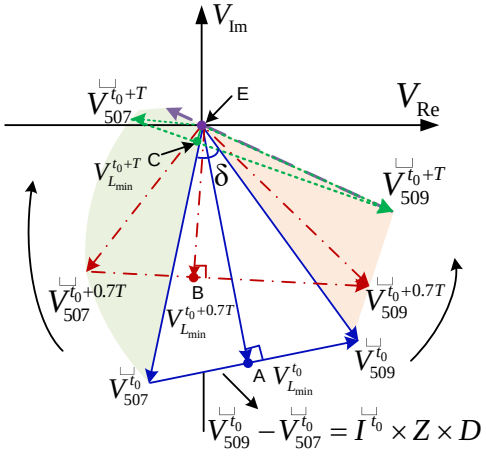

(b) Voltage-vector diagram of Buses 507 and 509

Fig. 7 Voltage-vector trajectory method for voltage profile analysis

With these explanations, it is time to further clarify the voltage traces during the network separation. It is assumed that the overall process takes T seconds. For any intermediate situation, e.g. at the time instance $t_0 + 0.7 \cdot T$ [indicated by dark red dash-dot vectors in Fig. 7(b)], $\vec{V}_{507}$ and $\vec{V}_{509}$ were rotated away from each other with more reduction in $\vec{V}_{507}^{t_0+0.7T}$ magnitude. The most noticeable change is that the lowest voltage of the line $\overrightarrow{EB}$ was considerably reduced from $\overrightarrow{EA}$. At the time $t_0 + T$ (indicated by green dot vectors), with further angular difference and $\vec{V}_{507}^{t_0+T}$ magnitude reduction, the lowest voltage of the line $\overrightarrow{EC}$ became substantially smaller – virtually a fault at point C (the electrical center), and the location of C was much closer to Bus 507 than that to Bus 509. If the angular difference advances to 180° as depicted by the purple dash vectors, the point E will be a clear virtual fault point with a close distance to Bus 507.

Fig. 8 shows the bus voltage magnitudes during the 2016 SA blackout. Geographically, South East (Bus 509) is located equally far away from both TIPS in SA and Latrobe Valley generation clusters from the VIC side, however, the use of 500 kV lines in VIC makes the line impedance relatively smaller, which means the Bus 509 voltage is much stiffer than that of Bus 507. Based on the voltage-vector trajectory method in Fig. 7, the following remarks can be made:

(1) *Voltage separation (16:18:15 – 16:18:15.8)*: Based on the relative stiffness of the buses, the Bus 315 and Bus 509 should hold voltage at a better level than Bus 507. The Bus 315 voltage trace should be first separated from the others, and then Bus 509 will be the second.

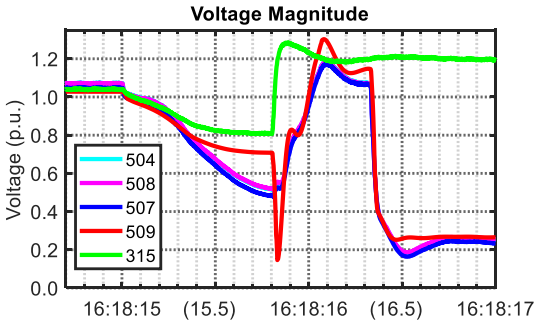

Fig. 8 Network status during the system blackout period

(2) *Network bottleneck (16:18:15 – 16:18:15.8)*: According to the voltage-vector trajectory method, the virtual fault location gradually became closer to Bus 507, and as a result, the Bus 507 voltage magnitude dropped at a faster speed than that of Bus 509 towards the end of the network separation. This indicates that the bottleneck of the network is located between Bus 509 and Bus 507. Therefore, series compensation may be done at the middle of the South East-to-Para connection as a solution to reduce network separation risk.

B. Over-Voltage Issue after Network Separation

Historically, after SA was isolated from the rest of the network, there was an incident with a high voltage level at South East. In the 2016 SA blackout, the voltage exceeded 1.2 pu, which immediately triggered the LGPS over-voltage protection. This reduced the on-line synchronous machines from 5 to 3, which further exacerbated the network imbalance.

The reason for such an over-voltage issue potentially lies in the Ferranti effect for long transmission lines. On one hand, the South East-to-Para lines are almost 450 km long, so it naturally has a large line charging capacitance (B), which raises the terminal voltage. On the other hand, long lines normally need reactive power devices for maintaining voltage levels at both ends. For example, capacitor banks and SVCs are installed in South East and Para substations for voltage support (similar to the impact of line charging capacitance).

After the network separation, as the voltage recovered from a very low level (Fig. 8), it was effectively energizing the South East area, which typically has a low load. Considering the large line charging capacitance, substation capacitor banks and SVCs, over-voltage during energization was expected. To further confirm this analysis, the line charging capacitance is reduced from 0.90 pu (original line parameter) to 0.10 pu for a comparison study as shown in Fig. 9. In order to compare the result under the same condition, the LGPS over-voltage trip was disabled in this part. From the simulation, over-voltage during recovery was effectively mitigated with a lower capacitance level.

It is noticed from Fig. 9(a) that when B is 0.90 pu, the peak voltage rises to approximately 1.31 pu. However, it decreases to around 1.16 pu with the reduced value of B as illustrated in Fig. 9(b). Therefore, these two peak voltages have a significant difference between them.

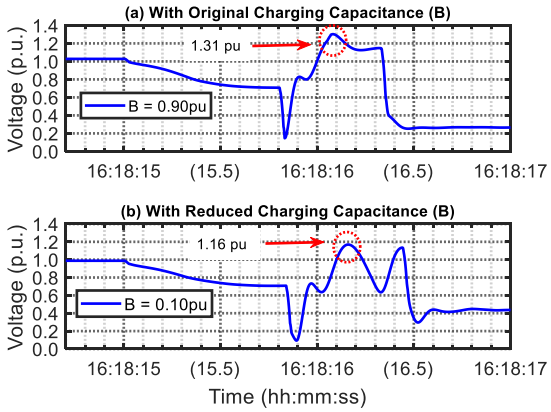

Fig. 9 Voltage profile comparison with different line charging capacitances

C. High ROCOF Induced Pole Slip Concern

In 2013, KEMA published a report [15] for EirGrid, which concluded that a ROCOF of 2 Hz/s can cause pole slip for most of the synchronous machines, therefore system stability may consequently be at a risk. In 2016, AEMO has also expressed a similar concern regarding high ROCOF [23]. Since a ROCOF of over 6 Hz/s was observed in the 2016 SA blackout, pole slip concerns for the TIPS units have been mentioned many times in different forums.

Fig. 10(a) shows the simulation results of the TIPS stator and rotor angles with system ROCOF during the blackout period, where each TIPS unit was loaded to around 42.5% of its capacity. It is found that the angular separation between stator and rotor was less than 90°, which means no pole slip of rotor with respect to the stator occurred. This immediately brings one question – why did not pole slip happen even with such a high ROCOF? To analyze this question, swing equation and power-angle equation of TIPS shown by (5) and (6) are taken into account.

$$2.H.\frac{1}{f_o}.\frac{df}{dt} \cong P_m - P_e \tag{5}$$

$$P_e \cong \frac{|\overrightarrow{V_{stator}}|\cdot|\overrightarrow{E_{rotor}}|}{X_s} \cdot \sin(\delta) \tag{6}$$

where H is the inertia constant (in s), f_0 denotes the nominal frequency (in Hz), P_m refers to the mechanical input (in pu), P_e refers to the electrical output (in pu), $|\overrightarrow{V_{stator}}|$is the stator voltage magnitude (in pu), $|\overrightarrow{E_{rotor}}|$ is the internal EMF (rotor) voltage magnitude (in pu), X_s indicates the equivalent synchronous reactance (in pu) and δ is the angle between stator and rotor (in deg.). ROCOF (in Hz/s) in this paper is taken as $-\frac{df}{dt}$ in order to have the same sign with P_e.

According to (5), when the grid frequency quickly declines, ROCOF $(-\frac{df}{dt})$ will drastically increase. This requires a significant rise of P_e since P_m cannot be rapidly changed. The additional P_e is effectively from the stored kinetic energy of the rotor (i.e. inertia response). As P_e increases, the angle δ subsequently increases as well according to (6). If the initial value of δ is not significantly high, it will not exceed 90° limit, which means there is no pole slip risk. Since the loading of TIPS units were only 42.5% during blackout ($\delta \approx 21°, \sin(\delta) \approx 0.36$), pole slip did not occur [Fig. 10(a)].

Fig. 10(b) depicts the TIPS stator and rotor angles with system ROCOF, when TIPS units are loaded to 92.5% of their capacities ($\delta \approx 38°, \sin(\delta) \approx 0.62$). It can be observed that the separation between stator and rotor angles increases to around 250° when ROCOF is around 6 Hz/s (marked by dark-red circles). This indicates that there is a potential rotor pole slip with respect to the stator.

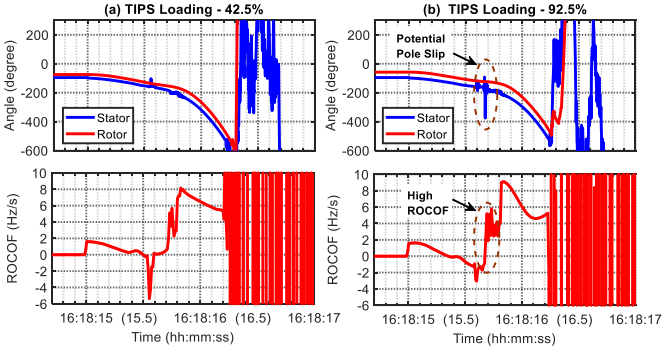

Fig. 10 TIPS pole slip potentials under low and high loading conditions

D. UFLS Malfunction due to Frequency Dip

As soon as the measured data of the SA blackout has been released, the frequency profiles as Fig. 2(a) have attracted significant amount of attention – mainly due to the mysterious frequency dip. Apart from the major concern on UFLS malfunction presented in Section I Part C Point (4), there have been a series of other issues around this frequency dip. What have caused such an intricate frequency trace – sudden changes in voltage phase and load? If the loss of synchronism relay separated the network at a slightly different time (with a different voltage angle), would the frequency dip be consistently observed or instead changed to a sharp frequency rise? Is the frequency profile a true reflection of the system frequency? If not, what is the actual grid frequency? Can UFLS be benefited from the improvement of obtaining the true frequency?

Currently, frequency measurement is heavily relying on PLL, therefore, analysis of the frequency trace should focus on widely applied PLL approaches. In theory, PLL depends on Direct-Quadrature-Zero (DQ0) transformation and feedback control with traditional Proportional–Integral (PI) controller. As a result, PLL is sensitive to sudden phase angle difference.

Based on re-construction of the SA blackout event, the findings are summarized as follows.

(1) As shown in Fig. 11(a), the frequency dip was very rapid after the network separation. It can be observed from Fig. 11(b), there was not any sudden phase angle change during this short period of time. Further, the voltage magnitudes almost remain the same, so there was no rapid load change either.

(2) As illustrated in Fig. 11(a), different relay delay (or voltage angle) at the separation did not cause any obvious changes in the frequency profiles. Therefore, the conventional three-phase PLL scheme is reasonably immune to voltage angle differences during the relay tripping.

(3) It is also noticed from Fig. 11(a) that the PLL estimated frequency can successfully track the grid frequency (TIPS synchronous frequency) when the dynamics are slow. However, under quick and large dynamic conditions, the PLL frequency cannot represent the actual network frequency. As indicated in Fig. 11(a), both frequencies dropped below the UFLS triggering frequency (49 Hz) nearly at the same time. Therefore, there is no substantial advantage of gaining the actual frequency for UFLS during the SA blackout, as the

UFLS timer will only start slightly earlier than that with PLL.

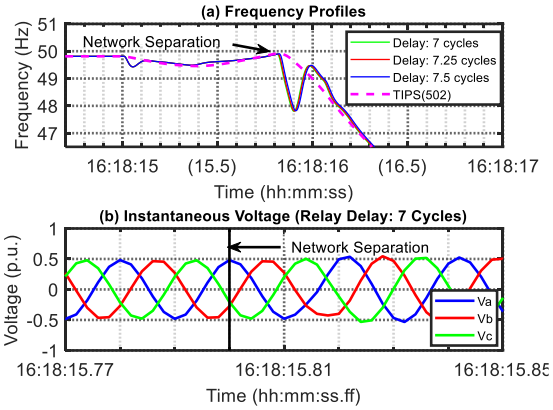

Fig. 11 System response with different relay delay time, and comparison between TIPS frequency and PLL frequency output

(4) As illustrated in Fig. 12, the error signal V_q drastically dropped after network separation, which caused a sharp decrease in PI controller output and hence PLL frequency estimation. This is due to the voltage wave shape distortion as depicted in Fig. 11(b). The extended grid voltage waveform quickly created an angle difference between the internal PLL phase and the network voltage phase, thus a rapid reduction of V_q was observed. As a result, the PLL frequency swiftly declined to catch up with the distorted voltage wave. It should be noted that due to PI controller characteristics, it is inevitable to have frequency overshoot after the frequency dip.

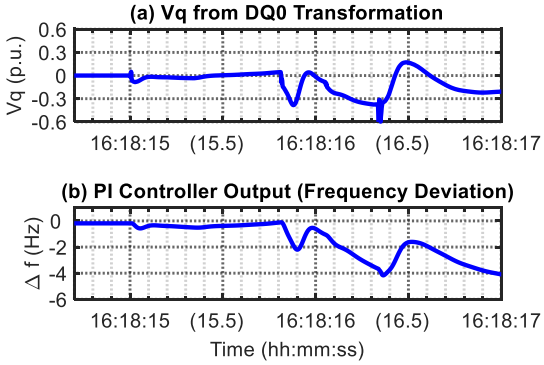

Fig. 12 Internal response of PLL

E. Frequency/Voltage Instability Debate

Since the 2016 SA blackout, there has been a continuation of debate in the industry on the true cause of the catastrophic event – frequency or voltage instability? Traditionally, the entire Southeast Australian grid has been regarded as a thin and long radial network hence requiring sufficient reactive power support. Many previous incidents of regional system collapse have been due to voltage instability [1]. Therefore, based on the LGPS over-voltage trip and the voltage curves after the network separation shown in Fig. 2(b), the voltage instability theory has been accepted by some engineers in the power industries.

Voltage instability is generally caused by inadequate reactive power compensation, which further affects voltage recovery, load carrying capability and so on [24]. Hence, the capacity of the SVCs at the two key locations (Para and South East) has been significantly increased – tripled in size. Moreover, in order to support both real and reactive power, the two LGPS synchronous machines are kept online with their over-voltage protection disabled. However, as revealed from the simulation results in Fig. 13, additional reactive power support did not provide any creditable improvement to the system. As soon as the SA network frequency dropped below the lower threshold of 47 Hz, the synchronous generators tripped, and the grid voltage became unstable soon afterwards. Therefore, the state-wide blackout should have been caused by frequency collapse rather than voltage instability.

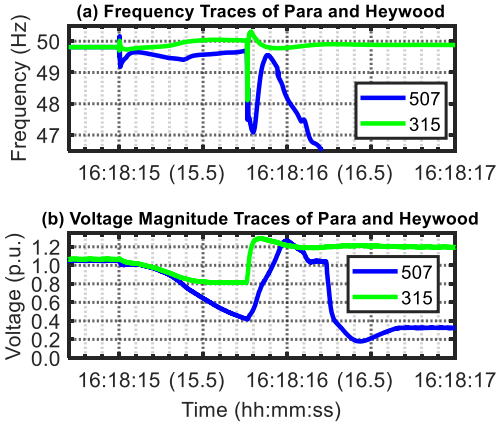

Fig. 13 Network performance with significantly increased reactive power support

IV. Potential Solutions to 2016 South Australia Blackout

As the important contributing factors for the 2016 SA blackout have now become clearer, potential solutions can be explored to improve the network resiliency.

A. Prevention of Blackout via Early Recognition of Network Separation

In the 2016 SA event, the network separation happened due to an excessive power import to SA via the Heywood interconnection. To deal with this issue, a new scheme is proposed in this section to identify a potential network separation at an early stage and subsequently apply certain load shedding to prevent the blackout. In addition, if the network separation still occurs even after the aforementioned load shedding, the chance for SA network to withstand such a separation would be considerably higher. This is due to the fact that the contingency size, ROCOF and SA generation-demand imbalance would be relatively lower since the load has already been reduced.

In the proposed scheme, at first a potential network separation is identified via a feature extraction technique. Afterwards, when the system features indicate that a network separation is going to happen, appropriate load shedding is applied to enhance the survivability of the system. Such a load shedding is named as an Improvised Load Shedding (ILS) in this paper.

Real time measurements provide an opportunity to recognize the network separation at an early stage. However, these measurements are one-dimensional time series, from which it is hard to distinguish the potential dynamic behaviors directly. Therefore, in this paper, the Minimum Volume Enclosing Ellipsoid (MVEE) method [25] is used to identify the voltage behaviors in real time by converting voltage magnitude signals to features of a multi-dimensional closed ellipsoid. Such ellipsoid with minimum volume is established by enclosing a certain part of the system

trajectory in the phasor measurement space. These features include centers (average voltage within specific time interval for each bus), ellipsoid volumes (representing the stress of the system), projections of the longest semi axis (variations of bus voltage) as well as the time derivative of the above parameters (evolution of system behaviors), which can provide a new perspective on system status. Then, these features are fed into Random Forest Classification (RFC) algorithm [26] to learn the underlying relationship between these features and system status, which are trained offline. After that, the trained model is applied to the network separation estimation in real time. Once a potential separation is identified, the ILS scheme is applied to improve the system survivability.

The methodologies to extract features of measured voltage magnitudes are as follows. At first, the measured bus voltages are expressed as (7).

$$\mathbf{V}=\begin{bmatrix} v_{11} & \mathrm{L} & v_{1m} \\ \mathrm{M} & \mathrm{O} & \mathrm{M} \\ v_{n1} & \mathrm{L} & v_{nm} \end{bmatrix},\ n<m \tag{7}$$

where v_{nm} are voltage magnitude at bus number n, m is the time instance of voltage measurement.

Next, in order to convert the one-dimensional voltage time series into multi-dimensional features of the closed ellipsoid, measured voltage magnitudes are constructed as (8) [27].

$$H_{A,c}=\{V\in\Omega^n|(V-c)^TA(V-c)\le 1\} \tag{8}$$

In (8), $H_{A,c}$ is an ellipsoid in a center form. Also, Ω^n is an n-dimensional space of the measured voltage magnitudes. Note that **c** and **A** are unknown quantities, where vector **c** denotes the center of the closed ellipsoid, and the positive definite matrix **A** determines the shape and orientation of the ellipsoid.

The ellipsoid volume, which is another vital feature, can be described by (9) – (11).

$$Vol\left(E_{\mathbf{A,c}}\right)=\pi^{n/2}/\Gamma\left(\frac{n+2}{2}\right)\sqrt{\det(\mathbf{A})} \tag{9}$$

$$\Gamma(n/2)=(n-2)!!\sqrt{n}/2^{(n-1)/2} \tag{10}$$

$$n!!=\begin{cases} n\times(n-2)\times\mathrm{L}\ 3\times 1, & n>0, odd \\ n\times(n-2)\times\mathrm{L}\ 4\times 2, & n>0, even \\ 1 & n=-1,0 \end{cases} \tag{11}$$

where Γ is a standard gamma function and the square root of the determinant of **A**, i.e., $\sqrt{\det(A)}$ is maximized subject to $\mathbf{c}\in\Omega^n$.

Then the MVEE problem can be described as (12) – (13).

$$\text{Objective function:}\quad \min\{Vol(E_{A,c})\} \tag{12}$$

$$\text{Constrains:}\quad (V-c)^TA(V-c)\le 1 \tag{13}$$

$$\mathrm{A}=A^T,\ \mathrm{A}>0$$

The objective function in (12) is deployed to find the enclosed ellipsoid with minimum volume while the constraints in (13) intend to ensure that all the measured voltage magnitudes are within the MVEE. This MVEE problem can be solved by the dual optimization problem proposed in [28].

After completing the ellipsoid construction, the projection of the longest semi axis, which is a desired feature, can be obtained through Singular Value Decomposition (SVD) as shown in (14). This feature indicates the dominant direction of the voltage change.

$$\mathbf{A}=\mathbf{PDQ}^{\mathrm{T}} \tag{14}$$

where $\mathbf{P}=[\mathbf{p_1},\mathbf{p_2},\mathrm{L}\ ,\mathbf{p_n}]$ and $\mathbf{Q}=[\mathbf{q_1},\mathbf{q_2},\mathrm{L}\ ,\mathbf{q_n}]^T$ are $n\times n$ eigenvectors. P are vectors in the direction of the measured voltage coordinated system, $\mathbf{D}=[\lambda_1,\lambda_2,\mathrm{L}\ \lambda_n]$ is a $n\times n$ diagonal matrix containing singular values $\lambda_1\ge\lambda_2\ge\mathrm{L}\ \ge\lambda_n$ of the matrix **A**. Therefore, the projection matrix of the ellipsoid on voltage measurement coordinates can be calculated by (15). In addition, the row in (15) with minimum λ_i is the projection of the longest semi axis.

$$R=\begin{bmatrix} p_{11}/\sqrt{\lambda_1} & \mathrm{L} & p_{1n}/\sqrt{\lambda_1} \\ \mathrm{M} & \mathrm{O} & \mathrm{M} \\ p_{n1}/\sqrt{\lambda_n} & \mathrm{L} & p_{nn}/\sqrt{\lambda_n} \end{bmatrix} \tag{15}$$

Furthermore, the derivative of the obtained features (center, volume and the projection of the longest semi axis) with respect to time, e.g., $\Delta Vol(E_{A,c})/\Delta\mathrm{t}$ are obtained to measure the general variation trend of the voltage magnitude.

Fig. 14 is the overall flowchart to identify the network separation based on MVEE. It mainly contains three steps:

(1) Informative features regarding power system status (separated/non-separated) are extracted from the measured bus voltage magnitudes after disturbance by MVEE.
(2) The extracted features are used to train the RFC algorithm [26] to learn the underlying relationship between the features and system status.
(3) The above trained RFC algorithm is further implemented to identify system status from the measured voltage traces.

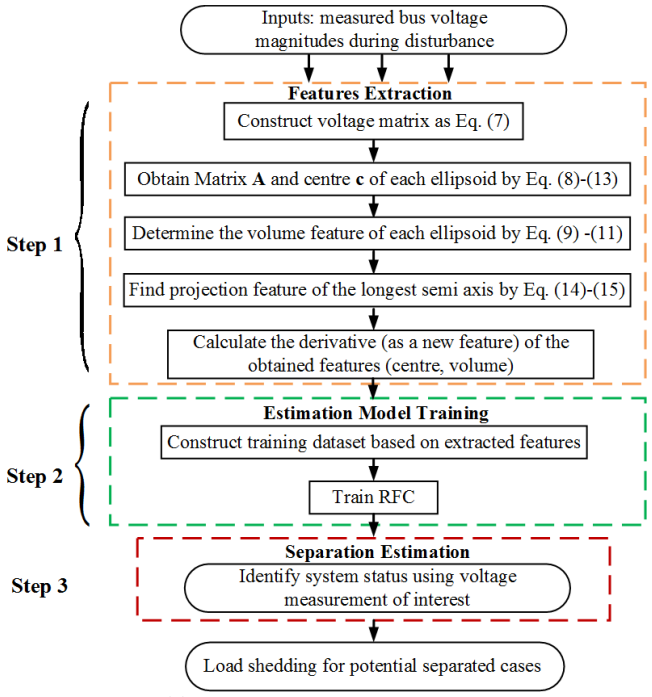

Fig. 14 Flowchart of feature extraction using MVEE

Fig. 15(a) shows an example of the voltage measurement from three buses – Bus-507, Bus-509 and Bus-315 during a disturbance, initiated at 0.5 s. The characteristic ellipsoid constructed from the voltage measurement using MVEE is presented in Fig. 15(b). The detailed process of constructing this ellipsoid is outlined below.

(1) Obtain the measured bus voltage magnitudes (Bus 507, Bus 509 and Bus 315) as time series data to construct

voltage matrix by (7) in each 0.1 s (time window for one ellipsoid) after the disturbance.

(2) Construct matrix **A** and center **c** of the ellipsoid via (8) – (13);

(3) Determine the volume feature of each ellipsoid by (9) – (11).

(4) Find the projection feature of the longest semi axis of the ellipsoid using (14) – (15);

(5) Compute the derivative (as a new feature) of the relevant features (center and volume) and subsequently construct the ellipsoid for each time window.

The above steps are repeated in each time window (W_1, W_2, W_3, and W_4) to eventually construct the ellipsoid shown in Fig. 15 (b). It is to be noted that there are total 40 features including ellipsoid volumes, centers, projections of the longest semi axis and the time derivative of the volume and center. Ultimately, these 40 features are used as the inputs of the RFC algorithm to identify the system status.

In terms of the computational efficiency of the proposed system separation prediction algorithm, it mainly depends on two parts, i.e., offline training and online prediction. Usually, the offline training (features extraction by MVEE and deep learning by RFC) takes several seconds to be completed for the application considered in this paper. In contrast, the online prediction (feature extraction by MVEE) on the single segment requires only several milliseconds. Therefore, the proposed prediction approach can provide real-time estimation of the system separation based on the voltage measurements from multiple buses. The computer specifications for the study are as follows. The professor of the computer is Inter(R) Core(TM) i5-5300U CPU @2.30GHz, and the installed memory (RAM) is 8.00GB.

It is worth clarifying that the dimension of features extracted from the ellipsoid is not influenced by the system scale (e.g. total number of system buses, total demand etc.). Essentially, the dimension is determined by the number of the buses deployed to monitor the system behaviors, and the number of time windows to identify the system status (separated or non-separated).

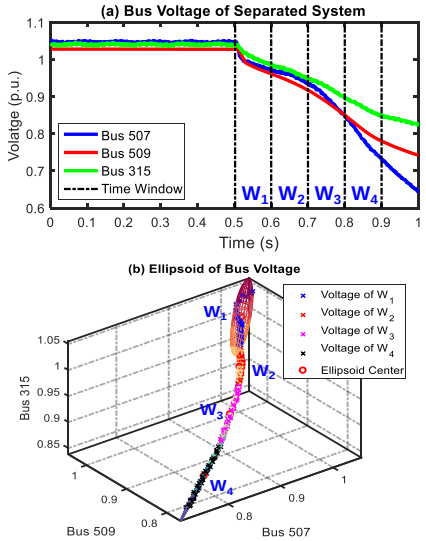

Fig. 15 Voltage ellipsoid for a disturbance applied at 0.5 second

To accomplish the estimation process, at first the dataset containing features extracted from voltage measurements of 50 simulation cases (21 separated cases and 29 non-separated cases) are taken into account. It is to be mentioned that the SA blackout event is not included in the above simulation cases. Next, these 50 cases are randomly divided into a training sub-dataset (70% samples) and a testing sub-dataset (30% samples). Then, the three steps as shown in Fig. 14 are applied to these datasets. Afterwards, the above procedures (dataset separation, training/testing) are repeated for 100 times. It is found that the average accuracy for system separation estimation is over 97%.

The trained estimation model is applied to the SA blackout, which successfully identifies the network separation at an early state – 16:18:15.4. Considering 0.1 s latency, ILS is applied at 16:18:15.5. The algorithm of applying the ILS is described as follows.

(1) To avoid any subsequent stability issues, the amount of ILS is gradually increased. It is assumed that at each stage, 50 MW load shedding is applied with a time delay of 50 ms.

(2) As soon as ILS is applied, SA frequency starts to improve. At the end of each stage, the network frequency is observed. If the frequency is still below a certain threshold (e.g. 49.85 Hz based on the Australian grid code [29]), another stage of ILS is deployed.

(3) The above process is continued until the moment when the SA frequency first reaches 49.85 Hz. Once the frequency is improved to this acceptable level, ILS is assumed to be stopped.

As shown in Fig. 16, the network separation and subsequent blackout is successfully prevented by applying the proposed strategy. It can be seen that both voltage and frequency traces recover satisfactorily after applying ILS. It is found that 250 MW ILS has been applied, which is around 14% of the total SA load. Finally, it is worth mentioning that potentially, the proposed scheme could also be applied to other power systems to mitigate the risk of blackouts.

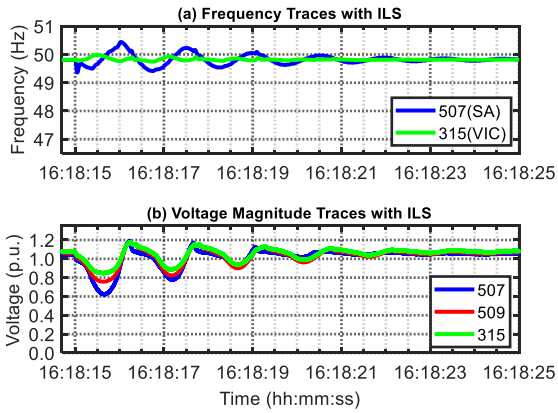

Fig. 16 Prevention of the SA blackout using the proposed scheme

In addition to the proposed scheme, there are other conventional techniques that can be explored to avoid the SA blackout. Such two techniques are discussed as follows.

B. Additional Series Capacitors between South East and Para

In order to avoid the network separation, series capacitors can be placed to the bottleneck of major transmission lines to reduce the overall circuit impedance and consequently increase power transfer capability. As identified in Section III Part A, since the bottleneck for the SA region lies between South East (Bus 509) and Para (Bus 507), series capacitors can be put in the middle of the lines to enhance the angular stability limit. Generally, such series compensation is kept within 80% of the line impedance due

to stability reasons [24]. Therefore, two levels of compensation – 20% and 50% have been considered.

Theoretically, both of the compensation levels are sufficient for the required 1,100 MW power flow. However, as shown in Fig. 17, the SA system collapses under the 20% compensation scenario. According to (3), this result is caused by the reduced power carrying capability of the lines between Bus 509 and Bus 507. Such a reduction is potentially due to the decrease of voltage magnitude caused by wind farm tripping. In contrast, the 50% compensation is sufficient even with declined voltages, and as a result the network separation and subsequent blackout can be avoided.

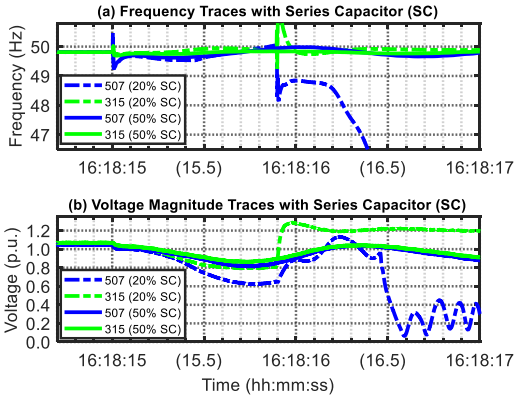

Fig. 17 Network performance with different amount of series capacitor compensation between South East (Bus 509) and Para (Bus 507)

It is to be articulated that higher series compensation increases the risk of sub-synchronous interaction (SSI), which is caused by wind machines (mainly Type 3 DFIG – Doubly Fed Induction Generator) with series capacitors in a (nearly) radial connection. Generally, there are four major techniques to mitigate this problem.

(1) Bypass filter across series capacitor: The sub-synchronous frequency components are selectively bypassed by a parallel filter containing a resistor, which can increase sub-synchronous damping or even prevent SSI [30].
(2) FACTS for oscillation damping: SSI can be alleviated by additional damping control of FACTS (Flexible AC Transmission System) devices, including TCSC (Thyristor Controlled Series Compensator), SVC (Static Var Compensator) and STATCOM (Static Synchronous Compensator) [31–32].
(3) Sub-synchronous Damper (SSD): Additional power electronic converters can be connected to wind farms to dissipate the resonance power of SSI [33]. The working principle is similar to an active filter, which absorbs (or counters) the sub-synchronous components.
(4) Controller modification: Extra damping controllers can be placed in RSC (Rotor Side Converter) and/or GSC (Grid Side Converter) within DFIG to mitigate SSI risks [34]. Moreover, passivity-based design [35–36] (e.g. time delay minimization, low integral gain for inner current loop, outer loop bandwidth reduction) can also be adopted to make wind farm more stable, which is equivalent to changing from constant power mode towards constant current mode.

Although Solution (1) is technically feasible, it is usually a very costly approach [30]. As for Solutions (2) and (3), they can be economically competitive since a) only a modest size is required [33, 37]; b) many wind farms and power networks already have SVC or STATCOM installed for reactive power support (e.g. as shown in Fig. 1, two large SVCs are operating at Bus 507 and Bus 509 in SA). Last but not the least, Solution (4) may be the most economical way of dealing with SSI [34], but it can become complicated when there are multiple manufacturers involved with different technologies [30].

Due to substantial wind penetration in SA, higher series compensation has risks of introducing SSI. As for the consequent SSI risks in SA, generally the frequency scanning method [38] will be first conducted to evaluate the potential SSI issues. Then practical and economical mitigation methods for the SA system can be explored as follows.

(1) Avoiding risky radial network layout with certain wind farm generation levels during dispatch and network maintenance.
(2) Adding damping control to existing SVCs and STATCOMs [Solution (2)].
(3) Retuning wind controllers since all the Type 3 wind generators in SA are from Vestas [Solution (4)].
(4) Deployment of SSD and bypass filter [Solutions (3) and (1)].

The SSI topic for the SA network can be a comprehensive study itself for another complete paper, so the detailed investigation on SSI is currently out of the scope of this paper.

C. Wind Emulated Inertia for Assisting UFLS

Additional inertia support can strengthen the network frequency response performance. To this end, the wind Emulated Inertia (EI) can be one of the most cost-effective methods. The inertia support from wind turbine generators is cost effective due to the following reasons.

(1) During normal operation, EI from variable-speed wind turbine generators is not enabled. It is activated to offer additional inertia support only during large frequency disturbances. In this paper, widely used GE WindInertia model is considered for EI function [39]. As shown in Fig. 18, the WindInertia controller takes grid frequency (f) as an input signal and compares it with the reference frequency (f_0). The resultant frequency deviation is then passed through a deadband. When this frequency deviation is larger than a preset threshold, EI response is activated.

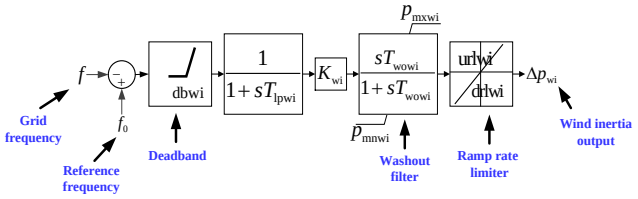

Fig. 18 GE WindInertia control model [39]

(2) Activation of wind EI does not require any power reserve during normal operation. Below rated wind speed, stored kinetic energy from a wind turbine rotor is temporarily offered to the grid, which is recovered later. At a higher wind speed, extraction of rotor kinetic energy and pitch control technique are subsequently deployed to provide EI response. Hence, there is no wind spillage cost during a normal operation.
(3) The EI response is almost energy neutral during the

contingency event, indicating that an increase in output power is followed by a decrease in output power. Therefore, no long-term financial concern is associated with the activation of wind inertia provision.

The wind EI may not significantly enhance the frequency nadir. However, owing to a supplementary inertia support, it decreases ROCOF. Consequently, it may provide more time for a UFLS action and governor response (or other real power response). Therefore, wind EI can improve the resiliency of a system, especially under high renewable penetration cases.

In order to clearly demonstrate the cost-effectiveness of wind EI, an example is considered where 600 MW Heywood interconnection tripping contingency is applied in the SA network. As shown in Fig. 19(a), frequency nadir is improved to 48.42 Hz (from 48.22 Hz) when EI from wind is activated. The corresponding power response curve of a 340 MW wind power plant is shown in Fig. 19(b). It can be observed that power output is temporarily increased by approximately 10% due to the activation of the EI controller. In addition, wind power output nearly recovers to its pre-contingency value (295 MW) after the required supporting period. It represents the energy neutral nature of the wind EI during a contingency event.

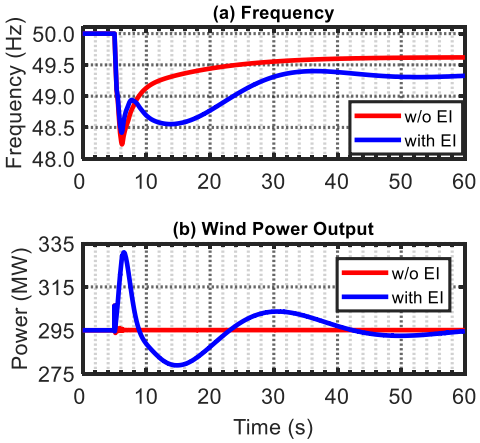

Fig. 19 Comparison of (a) frequency response and (b) wind power output

If all the wind farms are equipped with the EI function, it will enhance system survivability. During the SA blackout, the frequency dropped to 47 Hz very quickly due to a high ROCOF [Fig. 2(a)]. Therefore, it did not leave enough time for the deployment of UFLS and other real power response (e.g. governor response). Therefore, if ROCOF can be decreased by utilizing EI, the possibility of avoiding the blackout increases.

The SA UFLS starts at 49 Hz and ends before 47 Hz. The maximum amount of UFLS is 60% of the total load, and it has a time delay from 150 ms to 250 ms [12]. The SA frequency response for 150 ms UFLS delay is depicted in Fig. 20 (a). It can be seen that without EI, the frequency drops below 47 Hz, and eventually the SA grid collapses. On the other hand, due to the activation of EI, additional real power is supplied by wind power plants [Fig. 20(b)]. This extra support reasonably slows down the frequency response as shown by the blue trace in Fig. 20 (a). Eventually, the frequency excursion is stopped before 47 Hz with around 50% load shedding. Afterwards, the frequency starts to increase due to the sustained governor response from TIPS generators as depicted in Fig. 20(c). Ultimately, the frequency is rescued by the joint effort of UFLS and governor response, which indicates that the blackout is avoided due to EI support. Therefore, the activation of EI enhances the survivability of the SA network.

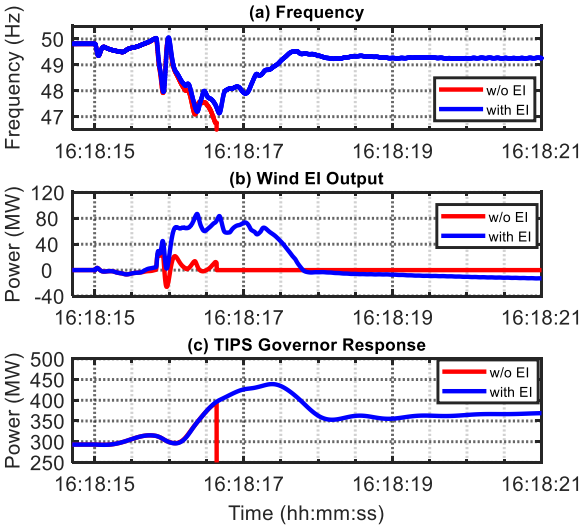

Fig. 20: Improvement of the SA network survivability with EI

It is to be mentioned that if UFLS delay is further increased to 250 ms, the SA frequency is not saved even with EI. This is due to the fact that for a longer time delay, speed of load shedding becomes slower. As a result, a power balance is not reestablished in time, and eventually the frequency excursion is not stopped. Therefore, prevention of the blackout with wind EI cannot be guaranteed at all times.

D. Discussion on Other Potential Solutions

Admittedly, there are other potential solutions to prevent the SA blackout. These include active wind power control [39], additional synchronous condensers [40], UFLS based on ROCOF [12], Murraylink HVDC frequency response [12], and battery storage [12]. Analysis of these methods is beyond the purpose of this paper, and this topic will be investigated in our future research work.

V. Conclusions

This paper analyzes the unsolved critical issues of the 2016 South Australia blackout, which is the first ever reported blackout incident due to high renewable penetration. In addition, it provides some potential solutions to prevent the SA blackout. The analysis is built on the reproduction of the blackout event with dynamic performances closely matched with the observation and measurement, which forms a reliable basis for the subsequent examination of various scenarios with different system settings. This research will be complementary to the official report from AEMO for clarification of a number of important and yet unexplained issues.

According to the investigations in this paper, the following conclusions can be made.

(1) Through the developed voltage-vector trajectory method, the virtual fault point (electrical center) can be more intuitively determined. Then based on the stiffness and capacity of the two areas, voltage profiles can be explained, and the network bottleneck can be identified, which is located closer to Para rather than South East or Heywood.

(2) Based on the Ferranti effect for long transmission lines, the reasons for over-voltage are found to be the

existence of large charging capacitance of the lines and high reactive power support during an equivalent energizing period of the South East region after network separation.

(3) During the blackout period, no rotor pole slip with respect to the stator took place in TIPS, even under very high ROCOF situation. This is due to the fact that the TIPS units were lightly loaded – around 42.5% of their capacities. However, if the generator loading was significantly increased (e.g. 92.5%), pole slip phenomenon was likely to occur.

(4) The PLL mechanism and voltage distortion after the network separation are the root causes of the frequency dip and surge, instead of sudden changes in phase angle and load. The resultant frequency profile is common for conventional PLL schemes, irrespective of voltage angles during separation. Moreover, such a frequency trace is not a true reflection of the actual grid frequency; however, obtaining the real frequency does not provide a distinct benefit for UFLS actions during the blackout.

(5) A substantial amount of reactive power support has been added into the SA network; however, this modification results in very little change in dynamic performances, which is unable to prevent the blackout. Therefore, the SA blackout was caused by frequency collapse of a low-inertia and low-reserve network with high renewable penetration, instead of voltage instability.

(6) The early recognition of network separation and subsequent deployment of improvised load shedding can successfully prevent the SA blackout scenario.

(7) Series capacitors installed between the bottleneck (Para-South East) can potentially avert the network separation and hence the state-wide blackout. However, possible power flow capability drop by temporarily reduced voltages should be considered. Therefore, a higher compensation is preferred.

(8) The wind emulated inertia method can cost-effectively provide inertia support and leave more time to assist the activation of UFLS and governor response, which could ultimately improve the survivability of the SA network. However, for a longer UFLS delay, such survivability cannot be guaranteed.

VI. References

[1] O. P. Veloza and F. Santamaria, "Analysis of major blackouts from 2003 to 2015: classification of incidents and review of main causes," The Electricity Journal, vol. 29, no. 7, pp. 42-49, 2016.

[2] C. J. Mozina, "A shot in the dark" IEEE Industry Applications Magazine, vol. 14, no. 5, pp. 45-52, 2008.

[3] G. Andersson, P. Donalek, et al., "Causes of the 2003 major grid blackouts in North America and Europe, and recommended means to improve system dynamic performance", IEEE Transactions on Power Systems, vol. 20, no. 4, pp. 1922-1928, 2005.

[4] A. Martins, P. Gomes, et al., "Lessons Learned in Restoration from Recent Blackout Incidents in Brazilian Power System", in CIGRE Paris Conference, Paris, France, 2012.

[5] V. Rampurkar, P. Pentayya, et al., "Cascading Failure Analysis for Indian Power Grid", IEEE Transactions on Smart Grid, vol. 7, no. 4, pp. 1951-1960, 2016.

[6] PJT, "Report on blackout in Turkey on 31st March 2015", 2015. [Online] Available: https://www.entsoe.eu/Documents/SOC%20documents/Regional_Groups_Continental_Europe/20150921_Black_Out_Report_v10_w.pdf

[7] Australian Demographic Statistics, December 2016. [Online] Available: http://www.abs.gov.au/ausstats/abs@.nsf/mf/3101.0

[8] ABC NEWS, "South Australian blackout costs business $367m, fears summer outages on way, lobby group says" [Online]. Available: http://www.abc.net.au/news/2016-12-09/sa-blackout-costs-could-have-been-worse-business-sa-says/8106600

[9] AEMO, "South Australian Demand Forecasts", 2016. [Online] Available: https://www.aemo.com.au/-/media/Files/Electricity/NEM/Planning_and_Forecasting/SA_Advisory/2016/2016_SA_Demand_Forecasts.pdf

[10] AEMO Generation Information Page, 2017 [Online]. Available: https://www.aemo.com.au/Electricity/National-Electricity-Market-NEM/Planning-and-forecasting/Generation-information.

[11] Australian Photovoltaic Institute, "Solar PV Status", 2017 [Online], Available: http://pv-map.apvi.org.au/historical#4/-26.67/134.12

[12] AEMO, "Black System South Australia 28 September 2016 – Integrated Final Report", March, 2017. [Online] Available: http://www.aemo.com.au/-/media/Files/Electricity/NEM/Market_Notices_and_Events/Power_System_Incident_Reports/2017/Integrated-Final-Report-SA-Black-System-28-September-2016.pdf

[13] M. Gibbard and D. Vowles, "Simplified 14-Generator Model of the SE Australian Power System", Revision 3, University of Adelaide, South Australia, June 2010. [Online] Available: http://www.eleceng.adelaide.edu.au/Groups/PCON/PowerSystems/IEE/BenchmarkData/Simplified_14-Gen_System_Rev3_20100701.pdf

[14] AEMO and ElectraNet, "Renewable Energy Integration in South Australia", 2014. [Online] Available: https://www.aemo.com.au/-/media/Files/PDF/Renewable_Energy_Integration_in_South_Australia_AEMO_Electranet_Report_Oct_2014.pdf

[15] DNV KEMA Energy & Sustainability, "ROCOF – An independent analysis on the ability of generators to ride through rate of change of frequency values up to 2Hz/s", February, 2013. [Online] Avaliable: http://www.eirgridgroup.com/site-files/library/EirGrid/DNV-KEMA_Report_RoCoF_20130208final_.pdf

[16] N.W. Miller, M. Shao, S. Venkataraman, C. Loutan and M. Rothleder, "Frequency Response of California and WECC Under High Wind and Solar Conditions", *in Proc. 2012 IEEE Power and Energy Society General Meeting*, pp.1-8.

[17] PSCAD/EMTDC, "Power System Computer Aided Design/Electromagnetic Transients including DC". [Online] Available: https://hvdc.ca/pscad/

[18] I. Mattsson, A. Ericsson, B. D. Railing, et. al, "Murraylink, the longest underground HVDC cable in the world", CIGRE Session 2004, pp. 1-8, 2004. [Online] Available: http://search-ext.abb.com/library/Download.aspx?DocumentID=03TS0394&LanguageCode=en&DocumentPartId=&Action=Launch, accessed on 10th Feb, 2018.

[19] Murraylink HVDC Light Interconnection, ABB Power Technologies. [Online] Available: https://library.e.abb.com/public/1456d376d330bbeac1256f4100489126/PT_MurrayLink.pdf, accessed on 10th Feb, 2018.

[20] AEMO and ElectraNet, "South Australia – Victoria (Heywood) Interconnector Upgrade, RIT-T: Project Assessment Conclusions Report", 2013. [Online] Available: http://www.aemo.com.au/media/Files/Other/planning/RITTs/SA_VIC_Heywood_Interconnector_Upgrade_RIT_T_PACR.pdf

[21] IEEE Tutorial on the Protection of Synchronous Generators, 2011 [Online] Available: http://www.pes-psrc.org/Reports/IEEEGenProtTutorial_20110506.pdf

[22] D. Reimert, *Protective Relaying for Power Generation Systems*, CRC Press, 2005, pp. 287-320.

[23] AEMO, "Future Power System Security Program", 2016 [Online]. Available: https://www.aemo.com.au/Electricity/National-Electricity-Market-NEM/Security-and-reliability/-/media/823E457AEA5E43BE83DDD56767126BF2.ashx

[24] P. Kundur, Power System Stability and Control, McGraw-hill, 1994.

[25] Yi Cui, Feifei Bai, Wenxuan Yao, Yong Liu, Ling Wu, Yilu Liu, "Power System Disturbance Localization using Recurrence Quantification Analysis and Minimum-Volume-Enclosing Ellipsoid", U.S. Patent Application No. 15/609,861.

[26] L. Breiman, "Random forest", Mach. Learn., vol.45, Issue 1, pp. 5-32, 2001.

[27] M. J. Todd and E. A. Yıldırım, "On Khachiyan's Algorithm for the Computation of Minimum-volume Enclosing Ellipsoids", Discrete Appl. Math., vol. 155, no. 13, pp. 1731–1744, Aug. 2007.

[28] P. Kumar, E. A.Yildirim, "Minimum volume enclosing ellipsoids and core sets", Journal of Optimization Theory and Applications, vol. 126, no. 1, pp. 1-21, July 2005.

[29] Australian Energy Market Commission, "National Electricity Rules Version 102, 2017 [Online]. Available: http://www.aemc.gov.au/Energy-Rules/National-electricity-rules/Current-Rules [Accessed: 19-Nov.-2017].

[30] J. Daniel, C. Han, et al., "ERCOT CREZ Reactive Power Compensation Study", ABB report (E3800-PR-00) for ERCOT, December, 2010.
[31] R. K. Varma, S. Auddy and Y. Semsedini, "Mitigation of Subsynchronous Resonance in a Series-Compensated Wind Farm Using FACTS Controllers", IEEE Transactions on Power Delivery, vol. 23, no. 3, pp. 1645-1654, 2008.
[32] A. Moharana, R. K. Varma and R. Seethapathy, "SSR Alleviation by STATCOM in Induction-Generator-Based Wind Farm Connected to Series Compensated Line", IEEE Transactions on Sustainable Energy, vol. 5, no. 3, pp. 947-957, 2014.
[33] L. Wang, X. Xie, Q. Jiang and X. Liu, "Centralised Solution for Subsynchronous Control Interaction of Doubly Fed Induction Generators Using Voltage-Sourced Converter", IET Generation, Transmission & Distribution, vol. 9, no. 16, pp. 2751-2759, 2015.
[34] A. E. Leon and J. A. Solsona, "Sub-Synchrnous Interaction Damping Control for DFIG Wind Turbines", IEEE Transactions on Power Systems, vol. 30, no. 1, pp. 419-428, 2015.
[35] L. Harnefors, X. Wang, A. G. Yepes and F. Blaabjerg, "Passivity-Based Stability Assessment of Grid-Connected VSCs - An Overview", IEEE Journal of Emerging and Selected Topics in Power Electronics, vol. 4, no. 1, pp. 116-125, 2016.
[36] L. Harnefors, M. Bongiorno and S. Lundberg, "Input-Admittance Calculation and Shaping for Controlled Voltage-Source Converters", IEEE Transactions on Industrial Electronics, vol. 54, no. 6, pp. 3323-3334, 2007.
[37] E. V. Larsen, "Wind Generators and Series-Compensated AC Transmission Lines", IEEE PES General Meeting, San Diego, CA, USA, 2012.
[38] B. Badrzadeh, M. Sahni, Y. Zhou, D. Muthumuni and A. Gole, "General Methodology for Analysis of Sub-Synchronous Interaction in Wind Power Plants", IEEE Transactions on Power Systems, vol. 28, no. 2, pp. 1858-1869, 2013.
[39] GE Energy, "Modelling of GE Wind Turbine-Generators for Grid Studies", Version 4.5, April 2010.
[40] N. Masood, R. Yan, T. K. Saha and S. Bartlett, "Post-Retirement Utilisation of Synchronous Generators to Enhance Security Performances in a Wind Dominated Power System", IET Generation, Transmission & Distribution, vol. 10, no. 13, pp. 3314-3321, 2016.

Ruifeng Yan (S'09, M'12) received the B. Eng. (Hons.) degree in Automation from University of Science and Technology, Beijing, China, in 2004, the M. Eng degree in Electrical Engineering from the Australian National University, Canberra, Australia, in 2007 and PhD degree in Power and Energy Systems from the University of Queensland, Brisbane, Australia, in 2012. His research interests include power system operation and analysis and renewable energy integration into power networks.

Nahid-Al-Masood (S'13, M'18) completed his B.Sc. and M.Sc. in Electrical and Electronic Engineering from Bangladesh University of Engineering and Technology (BUET), Dhaka, Bangladesh in 2008 and 2010 respectively. He earned the PhD degree in Power and Energy Systems from the University of Queensland, Brisbane, Australia, in 2017. His research interests include power system security and grid integration of renewable energy.

Tapan Kumar Saha (M'93, SM'97) was born in Bangladesh in 1959 and immigrated to Australia in 1989. He received his B. Sc. Engineering (Electrical and Electronic) in 1982 from the Bangladesh University of Engineering & Technology, Dhaka, Bangladesh, M. Tech (Electrical Engineering) in1985 from the Indian Institute of Technology, New Delhi, India and PhD in 1994 from the University of Queensland, Brisbane, Australia. Tapan is currently a Professor of Electrical Engineering in the School of Information Technology and Electrical Engineering, University of Queensland, Australia. He is a Fellow of the Institution of Engineers, Australia. His research interests include condition monitoring of electrical assets, power systems and power quality.

Feifei Bai (S'13, M'16) received the B.S. degree and Ph.D. degree in Power System and Automation from Southwest Jiaotong University, China, in 2010 and 2016, respectively. She was a joint-Ph.D. student at the University of Tennessee, Knoxville, USA, from 2012 to 2014. She is currently a postdoctoral research fellow in the School of Information Technology and Electrical Engineering, University of Queensland, Australia. Her main research interests are renewable energy integration into power grid, small signal stability analysis and wide-area damping control.

Huajie Gu received the B. Eng. degree in Automatic Control from Nanjing Technical University, Nanjing, China, in 2011, and the M. Eng. degree in Control Theory and Control Engineering from Tongji University, Shanghai, China, in 2014. Currently, he is a PhD student in the Power & Energy Systems Research Division at the School of Information Technology and Electrical Engineering, the University of Queensland, Australia. His research interests include wind turbine control and renewable power systems.